(Received 19 July 2025, Accepted 13 August 2025, Scheduled 24 August 2025)

Torque Ripple Reduction of the Anti-Disturbance Sliding Mode Deadbeat Control for Switched Reluctance Motors

Shining Lin[1], Aide Xu[2,*], Xiong Su[1], and Lidong Dong[1]

[1] College of Electrical Engineering of Ships, Dalian Maritime University, Dalian 116026, China
[2] College of Information and Science Technology, Dalian Maritime University, Dalian 116026, China

ABSTRACT: To improve the current and torque regulation performance of the traditional deadbeat predictive current control (DPCC) for switched reluctance motors under model parameter mismatch, this article proposes an improved DPCC method based on the sliding mode strategy. First, a dedicated torque-current converter is formulated to achieve precise transformation of electromagnetic torque into corresponding q-axis current references. Second, a unified anti-disturbance sliding mode control compensation scheme is introduced into both the torque-current converter and the deadbeat controller to mitigate the negative effects of model parameter mismatch on current and torque control. This integration achieves indirect torque control through phase current modulation, effectively reducing torque ripple. Furthermore, the stability of the controller under model parameter mismatch conditions is rigorously demonstrated through Lyapunov stability analysis. Finally, the effectiveness of the proposed control method is demonstrated through simulation results, and its significant superiority in current control performance and torque ripple suppression is shown.

1. INTRODUCTION

In recent years, switched reluctance motors (SRMs) have gradually highlighted their competitive advantages in various industrial applications due to their simple structure, rare-earth free, and high starting torque characteristics [1]. To achieve a fast dynamic response and improve the steady-state accuracy in SRMs, researchers have proposed many current control methods to suppress torque ripple, such as current chopper control, proportional-integral (PI) control, predictive control, and sliding mode control [2–5]. With the enhancement of microprocessor computing power, the discrete model-based deadbeat predictive current control is able to deal with complex nonlinear problems and system constraints and achieves a wide range of applications in the field of current loop regulation [6–8].

An accurate predictive modeling is effective in achieving fast convergence of DPCC and thus reducing steady state torque pulsations. Existing prediction models mainly include look-up tables method, iterative learning and genetic algorithm [9–11]. Typically, the effectiveness of these methods heavily relies on the accuracy of the torque-current inversion function, yet achieving high precision in this function faces significant technical bottlenecks. In [12], a new Q-learning scheduling method for current controllers is put forward, which achieves optimal tracking of reference currents through reinforcement learning method. In [13], a novel online torque-sharing function method is introduced. This approach dynamically generates phase current references by combining initial torque mapping with real-time decaying current sampling, effectively improving tracking accuracy. However, under high-speed conditions, the enhancement of back electromotive force may worsen current tracking errors, thus constraining torque control performance.

The performance of DPCC is directly limited by the precision of the motor modeling, which means that parameter errors or unmodeled dynamics can induce undesirable model mismatches. Existing studies address these limitations through two approaches: model correction [14, 15] and disturbance compensation [16, 17]. In [14], a digital Pulse Width Modulation (PWM) current controller is proposed, which employs parameter adaptive methods to online correct the SRM flux linkage model, thereby enhancing the robustness of DPCC systems. In [15], a recursive least squares estimator is designed and embedded within DPCC. This integration enables adaptive calibration of prediction models and optimally achieves current control objectives. In [16], a Kalman filter-based robust DPCC is developed to compensate for multi-parameter mismatches and mitigate periodic disturbances. In [17], an adaptive gain observer is incorporated into DPCC, demonstrating excellent current tracking performance even under significant modeling errors. However, existing model correction methods [14, 15] incur heavy computational burdens from real-time inductance estimation, while disturbance compensation methods [16, 17] require precise-model-dependent adaptive observers that treat mismatch as slow-varying disturbances, failing to handle fast dynamics and strong nonlinearity. Notably, the DPCC method based on a sliding mode disturbance observer has been successfully used to suppress model parameter disturbances in permanent magnet synchronous motors [18], but their directly decouplable state variables make them difficult to apply directly to SRM. The disturbance dynamics of SRM exhibit unique complexity, with disturbance terms intricately coupled to state variables such as $dq0$-axis voltages and $dq0$-axis currents.

* Corresponding author: Aide Xu (aidexu@dlmu.edu.cn).

To address the current control issues caused by model parameter mismatches in the DPCC system, this article introduces an enhanced DPCC method. On the one hand, a torque-current converter based on effective current vector mapping is designed for the coupling relationship between the electromagnetic torque and current of the motor, which provides a reliable reference current signal for the deadbeat controller. On the other hand, the method employs an anti-disturbance sliding mode controller to ensure robustness under parameter mismatch conditions. Compared with the existing methods [18], its unique feature is that it does not simply add a conventional observer but instead actively eliminates the influence of disturbances through a sliding mode predictive model. This method offers the advantages of simplicity in implementation and falls under the category of disturbance compensator-based control. The key contribution of this article is given as,

a) The outer loop uses a sliding mode torque-current converter based on effective current vector mapping as the front end of the DPCC, directly correcting the q-axis reference current using the sliding mode surface of the torque difference, thereby satisfying the saturation condition.

b) The inner loop modifies the DPCC voltage prediction law into a sliding mode compensation law for the first time, using the sliding mode surface of the current difference to real-time offset parameter mismatch disturbances and providing a unified convergence law, enabling single-step tuning of dual-loop gains.

2. SRM MODEL

The electromagnetic torque equation of the SRM in the three-phase stationary coordinate system is as follows:

$$T_e = \frac{N_r}{2}\left(\frac{\partial L_a}{\partial \theta_e} i_a^2 + \frac{\partial L_b}{\partial \theta_e} i_b^2 + \frac{\partial L_c}{\partial \theta_e} i_c^2\right) \tag{1}$$

where N_r is the number of rotor poles; i_a, i_b, i_c, L_a, L_b, and L_c are the phase current and phase inductance in stationary coordinates, respectively; T_e is the electromagnetic torque.

Neglecting the magnetic saturation, the a-phase inductance characteristics are expressed in terms of first-order Fourier series as:

$$L_a(\theta_e) = l_0 + l_1 \cos(\theta_e) \tag{2}$$

where l_0 and l_1 are the DC inductance and the first-order self-inductance amplitude, and θ_e is the electric rotor position.

According to Eq. (2), the voltage balance equation of the SRM in the $dq0$ coordinate system is given by:

$$\mathbf{u}_{dq0} = R\mathbf{i}_{dq0} + \mathbf{B}_0 \frac{d\mathbf{i}_{dq0}}{dt} + \omega_e \mathbf{C}_0 \mathbf{i}_{dq0} \tag{3}$$

where $\mathbf{u}_{dq0} = [u_d \ u_q \ u_0]^T$, $\mathbf{i}_{dq0} = [i_d \ i_q \ i_0]^T$,

$$\mathbf{B}_0 = \begin{bmatrix} l_0 + \frac{l_1}{2}\cos 3\theta_e & -\frac{l_1}{2}\sin 3\theta_e & \frac{l_1}{\sqrt{2}} \\ -\frac{l_1}{2}\sin 3\theta_e & l_0 - \frac{l_1}{2}\cos 3\theta_e & 0 \\ \frac{l_1}{\sqrt{2}} & 0 & l_0 \end{bmatrix},$$

$$\mathbf{C}_0 = \begin{bmatrix} -l_1 \sin 3\theta_e & -l_0 - l_1 \cos 3\theta_e & 0 \\ l_0 - l_1 \cos 3\theta_e & l_1 \sin 3\theta_e & \frac{l_1}{\sqrt{2}} \\ 0 & 0 & 0 \end{bmatrix}.$$

u_d, u_q, u_0, i_d, i_q, and i_0 are the voltage and current components of the $dq0$-axis. R is the stator resistance. ω_e is the electrical angular velocity, and the subscript "0" denotes the nominal value.

3. TRADITIONAL DPCC STRATEGY

3.1. DPCC Principle

Ignoring all disturbances, the deadbeat control law can be discretized from Eq. (3) using the first-order Euler formula, yielding the following expression:

$$\begin{aligned} \mathbf{u}_{dq0}(k) &= R\mathbf{i}_{dq0}(k) + \omega_e(k)\mathbf{C}_0(k)\mathbf{i}_{dq0}(k) \\ &\quad + \mathbf{B}_0(k)\frac{\mathbf{i}_{dq0}(k+1) - \mathbf{i}_{dq0}(k)}{T_s} \end{aligned} \tag{4}$$

where T_s is the sampling period, and k denotes the index of the kth sampling instant.

In the ideal conditions, the voltages generated by the predictive control ensure that the actual currents accurately track the reference current values at the beginning of the next control cycle, i.e., $i_{dq0}(k+1) = i^*_{dq0}(k)$. In addition, according to the theoretical results of torque per ampere control [19], the relationship between the reference current components of the $dq0$ axis is given by the following equation:

$$i_d^*(k) = 0, \quad i_0^*(k) = \sqrt{2} i_q^*(k) \tag{5}$$

The system block diagram of the traditional DPCC method is shown in Fig. 1. The deadbeat control law generates the inverter's switching signals through PWM, which are then input to an asymmetric half-bridge converter to drive the SRM for normal operation.

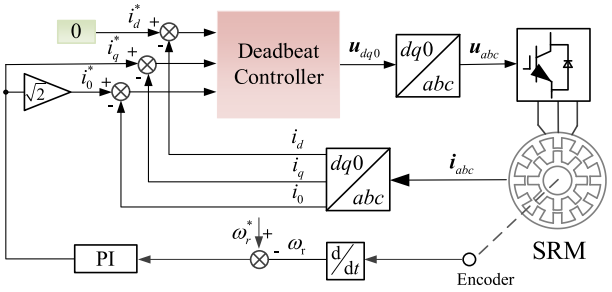

FIGURE 1. Block diagram of a conventional DPCC system.

3.2. Sensitivity Analysis under Parameter Mismatch

According to Eq. (4), it can be seen that constructing the DPCC system based on the idealized first-order inductance model has a strong dependence on the accuracy of the model parameters. During the actual operation of the motor, the temperature rise and magnetic saturation will lead to the mismatch between the controller parameters and the actual parameters of the motor, which in turn triggers the steady state current error.

Obviously, the DPCC system ignores magnetic saturation and unmodeled dynamics. In fact, considering that the actual values of the inductance parameters deviate from the nominal values, the deadbeat control law needs to introduce a disturbance term to characterize the effect of parameter mismatch. Therefore, the reconstructed model is as follows:

$$\mathbf{u}'_{dq0} = R\mathbf{i}_{dq0} + \omega_e \mathbf{C}_0 \mathbf{i}_{dq0} + \mathbf{B}_0 \frac{d\mathbf{i}_{dq0}}{dt} + \mathbf{F}_u \tag{6}$$

where $\mathbf{F}_u = [F_{u_d}\ F_{u_q}\ F_{u_0}]^T$ F_u is the disturbances due to model parameter mismatch and other model uncertainties, which is expressed as:

$$\mathbf{F}_u = R\mathbf{i}_{dq0} + \omega_e \Delta\mathbf{C}_0 \mathbf{i}_{dq0} + \Delta\mathbf{B}_0 \frac{d\mathbf{i}_{dq0}}{dt} \tag{7}$$

where $\Delta\mathbf{C} = \mathbf{C} - \mathbf{C}_0$ and $\Delta\mathbf{B} = \mathbf{B} - \mathbf{B}_0$.

The disturbances introduced above reveal the direct impact of inductance parameter deviations on the DPCC system. Specifically, $\Delta\mathbf{C}$ introduces the coupling term error, while $\Delta\mathbf{B}$ affects the accuracy of the current prediction.

According to Eq. (6), a discrete current model can be obtained as

$$\begin{aligned}\mathbf{i}_{dq0}(k+1) &= \mathbf{B}_0^{-1}(k)T_s\left(\mathbf{u}'_{dq0} + \mathbf{F}_u\right) \\ &+ \left[\mathbf{I} - \mathbf{B}_0^{-1}(k)T_s(R\mathbf{I} + \omega_e\mathbf{C}_0(k))\right]\mathbf{i}_{dq0}(k)\end{aligned} \tag{8}$$

where I is the identity matrix.

By associating Eqs. (8) and (4), the relationship between the current value at moment $k+1$ and the tracking reference current value is given by:

$$\mathbf{i}_{dq0}(k+1) = \mathbf{i}^*_{dq0}(k) + \mathbf{B}_0^{-1}(k)T_s\mathbf{F}_u \tag{9}$$

As shown in Eq. (9), the parameter mismatch causes an equivalent perturbation to be introduced in the current loop, so that the actual current and tracking reference current values cannot directly satisfy $\mathbf{i}_{dq0}(k+1) = \mathbf{i}^*_{dq0}$. Therefore, an anti-disturbance Sliding Mode Controller-based Deadbeat Predictive Current Control (ASMC-DPCC) method is presented in the next section to improve the robustness of the system under parameter mismatch.

4. ASMC-DPCC STRATEGY

4.1. Torque-Current Converter

In this section, a torque-current converter based on effective current vector mapping is introduced to replace the torque-current converter based on PI controller, thereby indirectly achieving torque control. Employing $i_d = 0$ strategy, the traditional q-axis current vector, which relies on three-phase current vector synthesis, is decomposed into two-phase current vectors to mitigate the adverse effects of continuous current in each winding within the negative torque region. By fixing the current vector i_q on the q-axis, Fig. 2 shows the mapping process of the effective current vector in a three-phase stationary coordinate system.

From Fig. 2, it is evident that the trajectory of the q-axis current vector is divided into three sectors. Within one electrical angle motion cycle, the current vector can be decomposed into adjacent two-phase currents in each sector. Hence, the three-phase currents are determined as follows:

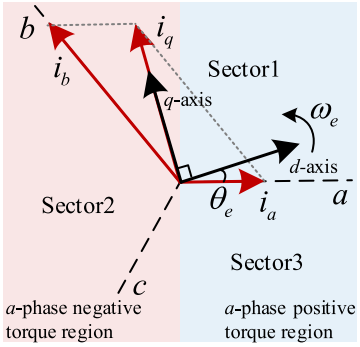

FIGURE 2. q-axis current vector mapping.

$$\mathbf{i}_{n\text{-}abc} = i_q \mathbf{D}_n, \quad n = 1, 2, 3 \tag{10}$$

where n indicates the sector where i_q is located. For example, $\mathbf{i}_{1\text{-}abc}$ means $i_{1\text{-}a}, i_{1\text{-}b}, i_{1\text{-}c}$ when i_q is located in sector 1.

$$\mathbf{i}_{n\text{-}abc} = \begin{bmatrix} \mathbf{i}_{1\text{-}a} & i_{1-b} & i_{1-c} \\ \mathbf{i}_{2-a} & i_{2-b} & i_{2-c} \\ \mathbf{i}_{3-a} & i_{2-b} & i_{3-c} \end{bmatrix}.$$

When θ_e falls within the intervals $[-2/\pi, \pi/6]$, $[\pi/6, 5\pi/6]$, $[5\pi/6, 3\pi/2]$, respectively, the expressions for D_1, D_2, and D_3 are as follows: $D_1 = [\sin(\pi/6 - \theta_e)/\sin(\pi/3)\ \cos(\theta_e)/\sin(\pi/3)\ 0]$, $D_2 = [0\ \sin(5\pi/6 - \theta_e)/\sin(\pi/3)\ \sin(\theta_e\pi/6)/\sin(\pi/3)]$, and $D_3 = [\sin(\theta_e - 5\pi/6)/\sin(\pi/3)\ 0\ -\cos(\theta_e)/\sin(\pi/3)]$.

By associating Eq. (1), Eq. (2), and Eq. (10), the estimated equation for the q-axis current without considering magnetic saturation can be constructed as:

$$\hat{i}_q = \sqrt{\frac{6T_e^*}{A_0}} \tag{11}$$

where $A_0 = N_r l_1(\sin 3\theta_e + 4\sin(\theta_e + 2(2-n)\pi/3))$, and T_e^* is the reference value of the electromagnetic torque.

The torque-current converter serves as the inverse torque model. In the deadbeat controller architecture, the current estimate is computed in real-time using Eq. (11) further decomposed into a reference current signal through q-axis current vector mapping which serves as the control input to drive the dynamic behavior of the system. Moreover, as shown in Fig. 2, the three-phase current references are continuous at the sector boundaries, and the resulting torque exhibits a smooth transition without spikes.

4.2. Design of ASMC-DPCC

In DPCC systems, model parameter mismatches are quite common and inevitably introduce steady-state current errors. This error seriously deteriorates the performance of the torque-current converter and deadbeat controller, leading to a decrease in control accuracy and an increase in torque ripple.

To further achieve indirect torque control under phase current regulation, a sliding mode surface is designed based on current and torque tracking errors as follows:

$$\begin{cases} \mathbf{s}_u = \mathbf{e}_u = \mathbf{i}^*_{dq0} - \mathbf{i}_{dq0} \\ s_i = e_i = T^*_e - T_e \end{cases} \tag{12}$$

where e_u is the current error matrix, e_i the torque error, and $\mathbf{i}^*_{dq0} = [i^*_d \ i^*_q \ i^*_0]^T$ the current reference for the $dq0$-axis.

The control functions $\mathbf{u}^*_{dq0} = [u^*_d \ u^*_q \ u^*_0]^T$ and $\hat{i}^*_q$ are associated with respective sliding mode compensation quantities with the following expressions:

$$\begin{cases} \mathbf{u}^*_{dq0} = \mathbf{u}_{dq0} + \mathbf{u}_{smcdq0} \\ \hat{i}^*_q = \hat{i}_q + i_{smcq} \end{cases} \tag{13}$$

where $\mathbf{u}_{smcdq0}$ and i_{smcq} indicate compensation for the disturbances caused by parameter mismatch. i_{smcq} simultaneously compensates for the estimated current error caused by the linear torque-to-current converter based on effective current vector mapping, rather than through an explicit nonlinear model.

Due to the strong coupling between disturbance terms and state variables such as $dq0$-axis voltages and $dq0$-axis currents, sliding mode compensation quantity is designed as a proportional feedback form of matrix error to offset the perturbation effect in real time, and its expression is as follows:

$$\begin{cases} \mathbf{u}_{smcdq0} = \mathbf{B}_0 \dot{\mathbf{s}}_u \\ i_{smcq} = l_1 \dot{s}_i \end{cases} \tag{14}$$

To simplify parameter design, both controllers adopt a unified reaching law design. When the current and torque errors are zero, the tracking is achieved. Therefore, this article designs the sliding mode reaching law as:

$$\begin{cases} \dot{\mathbf{s}}_u = -\eta_1 \text{sign}(\mathbf{s}_u) \left|\mathbf{s}_u\right| - \tau_1 \mathbf{s}_u \left|\mathbf{s}_u\right| \\ \dot{s}_i = -\eta_2 \text{sign}(s_i) \left|s_i\right| - \tau_2 s_i \left|s_i\right| \end{cases} \tag{15}$$

where η_1, η_2, τ_1, and τ_2 are the sliding mode gain, and sign is the switching function.

By solving Eqs. (12) to (15) simultaneously, the ASMC-DPCC model that accounts for parameter disturbance compensation can be obtained as follows:

$$\begin{cases} \mathbf{u}^*_{dq0} = \mathbf{u}_{dq0} - \mathbf{B}_0 \eta_1 \text{sign}(\mathbf{s}_u) \left|\mathbf{s}_u\right| - \mathbf{B}_0 \tau_1 \mathbf{s}_u \left|\mathbf{s}_u\right| \\ i^*_q = i_q - l_1 \eta_2 \text{sign}(s_i) \left|s_i\right| - l_1 \tau_2 s_i \left|s_i\right| \end{cases} \tag{16}$$

According to Lyapunov's stability theory, it is necessary to construct a Lyapunov function $V = 1/2 s^2$, whose derivative is given by the following expression:

$$\begin{cases} \dot{\mathbf{V}}_u = \mathbf{s}_u \dot{\mathbf{s}}_u = -\eta_1 \left|\mathbf{s}_u\right|^2 - \tau_1 \mathbf{s}_u^2 \left|\mathbf{s}_u\right| \\ \dot{V} = s_i \dot{s}_i = -\eta_2 \left|s_i\right|^2 - \tau_2 s_i^2 \left|s_i\right| \end{cases} \tag{17}$$

Since $\eta_1, \eta_2 > 0$, $\tau_1, \tau_2 > 0$ and $|\mathbf{s}_u|, |s_i| > 0$. It is evident that $\dot{\mathbf{V}}_u, \dot{V}_i \leq 0$, satisfying the conditions for global asymptotic stability.

By differentiating the sliding surface and combining it with the reconstructed voltage Eq. (6), the dynamic equation of the sliding surface is obtained as follows:

$$\begin{aligned} \dot{\mathbf{s}}_u &= \frac{d(\mathbf{i}^*_{dq0} - \mathbf{i}_{dq0})}{dt} = \frac{d\mathbf{i}^*_{dq0}}{dt} + \frac{R}{\mathbf{B}_0}\mathbf{i}_{dq0} + \frac{\omega_e \mathbf{C}_0}{\mathbf{B}_0}\mathbf{i}_{dq0} \\ &\quad - \frac{1}{\mathbf{B}_0}\mathbf{U}^*_{dq0} + \frac{1}{\mathbf{B}_0}\mathbf{F}_u \end{aligned} \tag{18}$$

By substituting the control functions into Eq. (18) of the sliding surface, the following expression is obtained:

$$\dot{\mathbf{s}}_u = \frac{d\mathbf{i}^*_{dq0}}{dt} - \frac{d\mathbf{i}_{dq0}}{dt} + \eta_1 \text{sign}(\mathbf{s}_u) \left|\mathbf{s}_u\right| + \tau_1 \mathbf{s}_u \left|\mathbf{s}_u\right| + \frac{1}{\mathbf{B}_0}\mathbf{F}_u \tag{19}$$

Furthermore, to ensure the stability of the deadbeat controller under parameter mismatches, constraints need to be imposed on the sliding mode gains η_1 and τ_1 to satisfy the relation $\mathbf{s}_u \dot{\mathbf{s}}_u < 0$.

Defining the composite disturbance upper bound $\mathbf{M} = \max |d\mathbf{i}_{dq0}/dt - d\mathbf{i}^*_{dq0}/dt - 1/\mathbf{B}_0\mathbf{F}_u|$, the constraints on η_1 and τ_1 are given by the following relation:

$$\begin{cases} \eta_1 < \frac{\mathbf{M} - \tau_1 \mathbf{s}_u^2}{\mathbf{s}_u}, & \mathbf{s}_u > 0 \\ \eta_1 < \frac{\mathbf{M} + \tau_1 \mathbf{s}_u^2}{\mathbf{s}_u}, & \mathbf{s}_u < 0 \end{cases} \tag{20}$$

In summary, the schematic diagram of the proposed anti-disturbance sliding mode controller is shown in Fig. 3, which includes the sliding mode torque-current converter for torque regulation and the sliding mode deadbeat controller to eliminate current tracking errors under parameter mismatch. The inputs of the sliding mode controller are the errors in torque and $dq0$-axis currents, while the outputs are the compensations for the q-axis current and deadbeat control law.

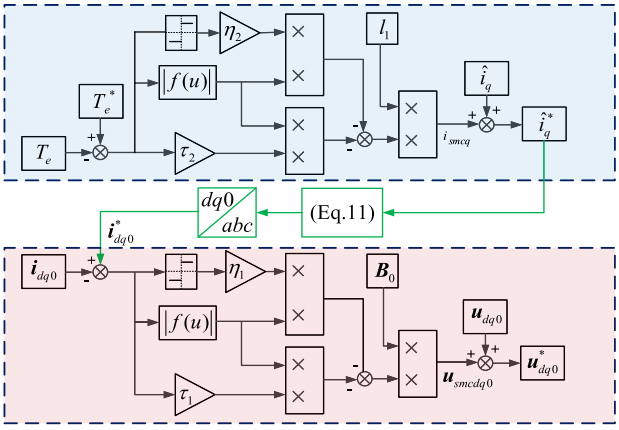

FIGURE 3. Schematic diagram of anti-disturbance sliding mode controller.

5. SIMULATION AND EXPERIMENTAL VERIFICATION

The block diagram of the ASMC-DPCC system is shown in Fig. 4. The reference current for the $dq0$ axis at the next moment is obtained based on the torque-current converter of the

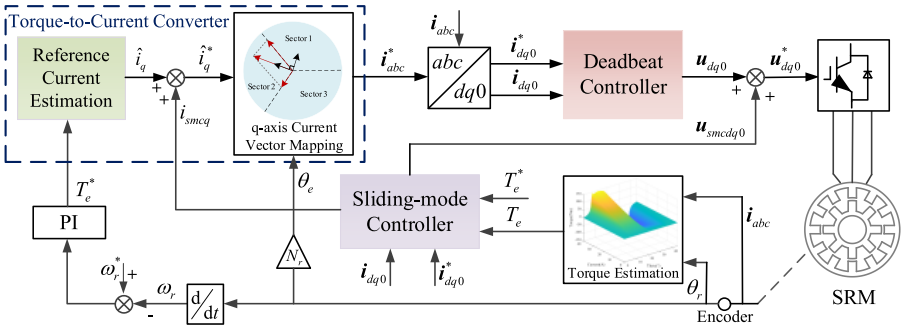

FIGURE 4. Block diagram of ASMC-DPCC system.

effective current vector decomposition. ASMC dynamic compensation parameters are used to compensate for interference, so that even when the model parameters are mismatched, it is still possible to solve for a deadbeat control law that meets the control requirements.

For SRM, relying solely on mathematical models to directly describe its torque characteristics often fails to meet the accuracy requirements of practical applications. Therefore, a torque table is established based on the stall test data of the locked rotor. Fig. 5 shows the measurement results of the torque model. The total torque is queried in real time through the torque table, thereby providing the control system with accurate electromagnetic torque data.

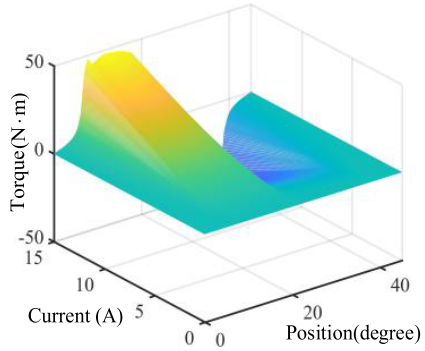

FIGURE 5. Torque model.

5.1. Simulation Results and Analysis

In this article, a simulation model is developed based on the parameters of a three-phase SRM. The specifications of the motor are presented in Table 1. The model parameters l_0 and l_1 are identified using only two sets of flux-linkage data obtained at two extreme rotor positions [20]. The DC inductance (l_0) is 150.2 mH, and the first-order self-inductance (l_1) is 129.8 mH.

TABLE 1. Specifications of the motor.

Parameter name	Values
Stator/rotor poles	12/8
Rated Power	55 kW
Rated torque	35 N·m
Rated current	11.3 A
Rated speed	1500 r/min
Stator resistance	1.472 Ω
Moment of inertia	0.0189 kg·m^2

Based on the stability and anti-disturbance constraints established in Section 4, the sliding mode gain coefficients are systematically determined. Setting τ_1 proportional to $1/T_s$ regulates the convergence trajectory of current errors. To ensure smooth torque dynamic response, the bandwidth of the torque loop is strictly constrained to be lower than that of the current loop, hence τ_2 is much smaller than τ_1. Simulation-based estimation of the disturbance upper bound M confirms the range for η_1. The torque compensation gain η_2 is directly associated with the q-axis tracking error of the current-torque converter to provide strong robustness margin. Therefore, the optimal control loop parameter for the proposed algorithm is set to $\eta_1 = 10$, $\eta_2 = 4$, $\tau_1 = 1000$, $\tau_2 = 1$.

The control performances of the different algorithms are compared using current error and torque ripple as metrics, whose formulas are given in Eq. (12) and Eq. (21), respectively.

$$T_r = (T_{\max} - T_{\min})/T_{avg} \tag{21}$$

where T_r is the torque ripple coefficient; $T_{\max}$, $T_{\min}$, and T_{avg} are the maximum, minimum, and average values of total torque, respectively.

When the model parameters are matched, the simulation comparison results of the three control methods at 1500 r/min with a 5 N·m load are shown in Fig. 6.

From Fig. 6(a), it can be seen that the torque ripple of the conventional DPCC method with the torque-current converter based on PI controller is 64.6%. As shown in Fig. 6(b), the torque ripple of the proposed ASMC-DPCC method is further reduced to 39.7%, confirming the excellent torque control performance of the torque-current converter based on current vector mapping under high-speed conditions.

Second, in order to assess the robustness of the proposed current control scheme under model parameter mismatch, comparative simulations are conducted for three control methods. These simulations introduce step changes in inductance parameters at 1000 r/min with a 10 N·m load. Specifically, at 0.25 seconds into the simulation, the inductance parameters l_0 and l_1 are abruptly decreased to 50% of their nominal values, and the steady-state response characteristics are shown in Fig. 7. By comparing the $dq0$ axis current tracking performance and torque ripple metrics, the differences in control performance between the matched and mismatched conditions of the model parameters are further quantified.

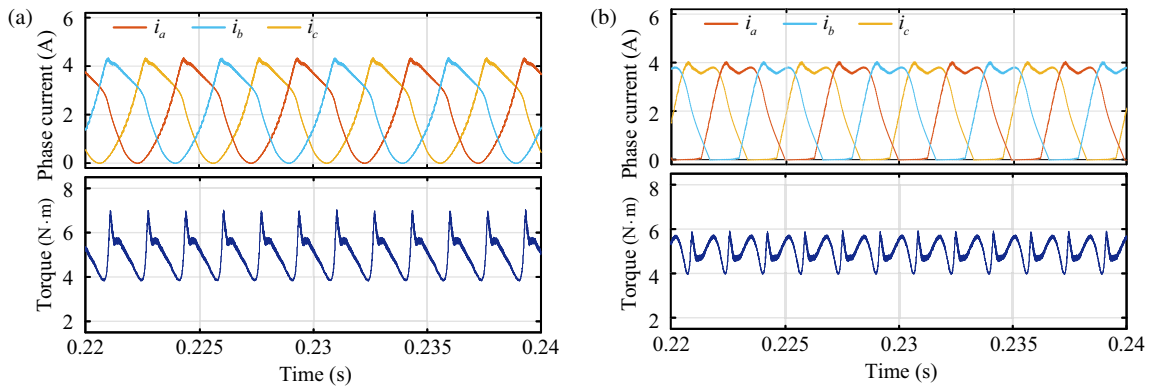

FIGURE 6. Comparison of simulation results at 1500 r/min with a 5 N·m load when model parameters are matched: (a) Traditional DPCC; (b) ASMC-DPCC.

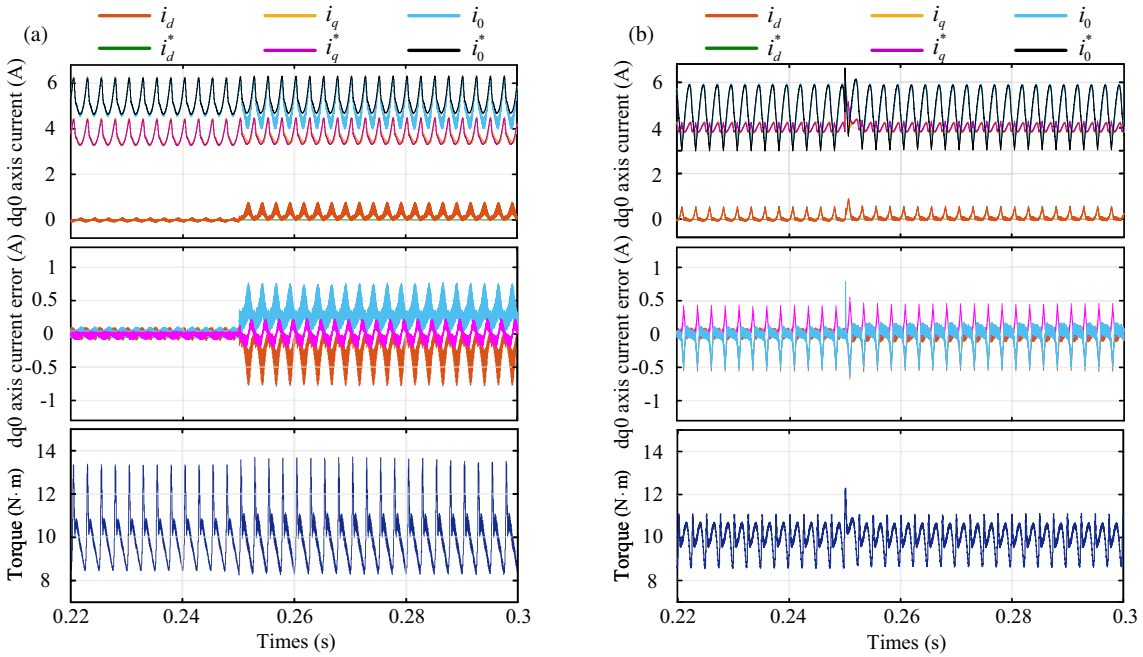

FIGURE 7. Comparison of simulation results at 1000 r/min with a 10 N·m load when model parameters are mismatched: (a) Traditional DPCC; (b) ASMC-DPCC.

The simulation results show that when the model parameters are matched, the $dq0$-axis current tracking of the three control methods performs well. However, the torque ripple characteristics differ significantly. The torque ripples of conventional DPCC and ASMC-DPCC are 49.5% and 24.8%, respectively, which shows that ASMC-DPCC method offers superior torque regulation performance.

The $dq0$-axis current tracking ability of both control methods decreases when the inductance parameters l_0 and l_1 undergo a step decrease. The maximum tracking error of the $dq0$-axis current of ASMC-DPCC increases by only 4.4 m A, 25 mA, and 5.6 mA, respectively, which can basically recover to the steady-state level when the parameters are matched. In contrast, the d-axis and 0-axis currents of the conventional DPCC show significant tracking deviations, with the maximum tracking error exceeding 0.78 A and 0.76 A, respectively, which are 0.69 A and 0.65 A higher than that of the inductance parameter matching, respectively. Specifically, underestimation of inductance parameters results in insufficient predicted voltage, causing the d-axis current to exhibit a negative steady-state error and the 0-axis current to trigger amplified positive fluctuations. The above phenomena show that the proposed sliding mode deadbeat controller suppresses the current tracking error by compensating for the voltage deviation.

After the motor parameters are mismatched, the conventional DPCC could not achieve accurate current tracking, and its stabilized torque ripple increases by 5%. In addition, the torque-current converter, due to parameter mismatch, operates in a non-equilibrium state at the moment of 0.25 seconds, triggering transient torque fluctuations. This phenomenon is allowed to be considered. The ASMC-DPCC is able to reduce the amplitude of transient torque fluctuations to 13 N·m, and the torque ripple remains at 24.85% after steady state. This is attributed to the fact that the strong nonlinearity of the SRM is treated as per-

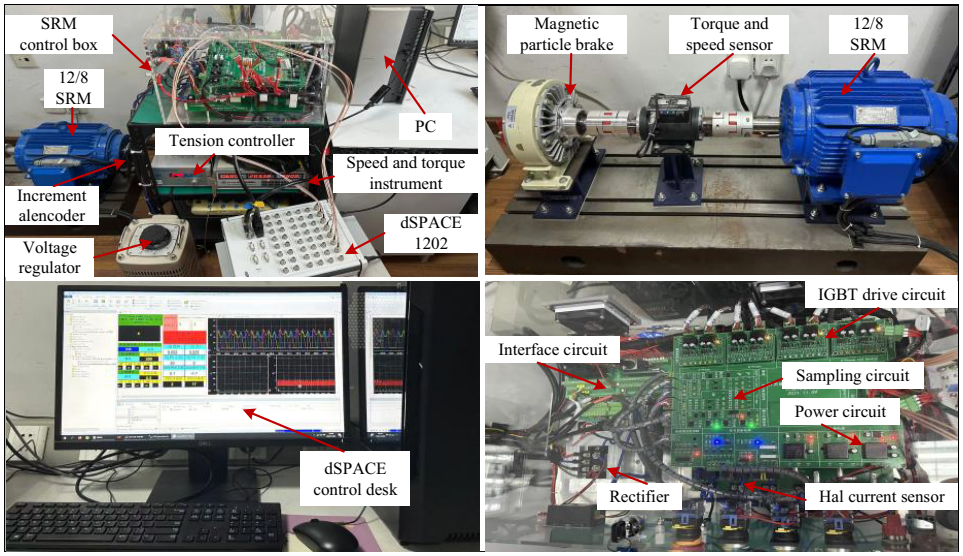

FIGURE 8. Experimental platforms.

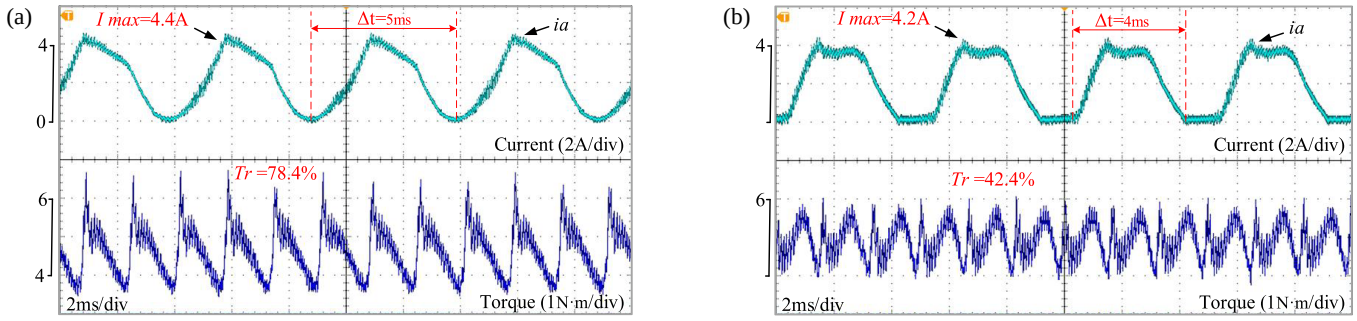

FIGURE 9. Comparison of experimental results at 1500 r/min with a 5 N·m load when model parameters are matched: (a) Traditional DPCC; (b) ASMC-DPCC.

turbations by the sliding mode torque-current converter during parameter mismatch, and its strong robustness suppresses the direct transmission of these disturbances to the torque, thus effectively regulating the torque through torque compensation.

5.2. Experimental Results and Analysis

Figure 8 shows the experimental platform of the constructed SRM drive system, which mainly consists of SRM control box, asymmetric half-bridge power converter, incremental encoder, magnetic powder brake, host computer, and dSPACE. The PWM sampling frequency of the differential beatless controller is set to 10 kHz, and the DC bus voltage is 200 V. The motor parameters and sliding mode gain coefficients are consistent with those in the simulation. The adopted conventional DPCC method and the proposed ASMC-DPCC method are consistent with Fig. 1 and Fig. 4, respectively.

Figure 9 shows the experimental results of phase current and torque of CC and ASMC-DPCC under parameter matching. When the motor is running at rated speed, the torque ripple of the conventional DPCC method reaches 78.4%, and the phase current peak ($I_{\max}$) is as high as 4.4 A. In contrast, the T_r of ASMC-DPCC method is suppressed to 42.4%, while $I_{\max}$ is reduced to 4.2 A. The ASMC-DPCC method has a significant advantage in reducing the torque ripple and current peak. Compared with the current strategy based on PI control, the torque-current converter based on the effective current vector mapping significantly reduces the $dq0$-axis cross-coupling effect, which linearizes the mapping relationship between the electromagnetic torque and q-axis current, thus suppressing the torque ripple.

In addition, Fig. 9 shows a comparison of the tail currents of the two methods. The results show that when the traditional DPCC method is used, each phase has a longer conduction time throughout the electrical cycle, resulting in higher source current consumption. It indicates that while the traditional DPCC method increases the conduction time, it also increases the current consumption of the system.

Figure 10 compares the experimental results of $dq0$-axis current and torque of DPCC and ASMC-DPCC under parameter mismatch. A comparison with Fig. 7 shows that the actual current on the $dq0$-axis in the experimental and simulated results shows the same trend. This is consistent with the expected magnetic saturation, inverter dead zone, and sensor dynamic effects, which are not considered in the model of Eq. (2) but are suppressed by the anti-disturbance sliding mode controller.

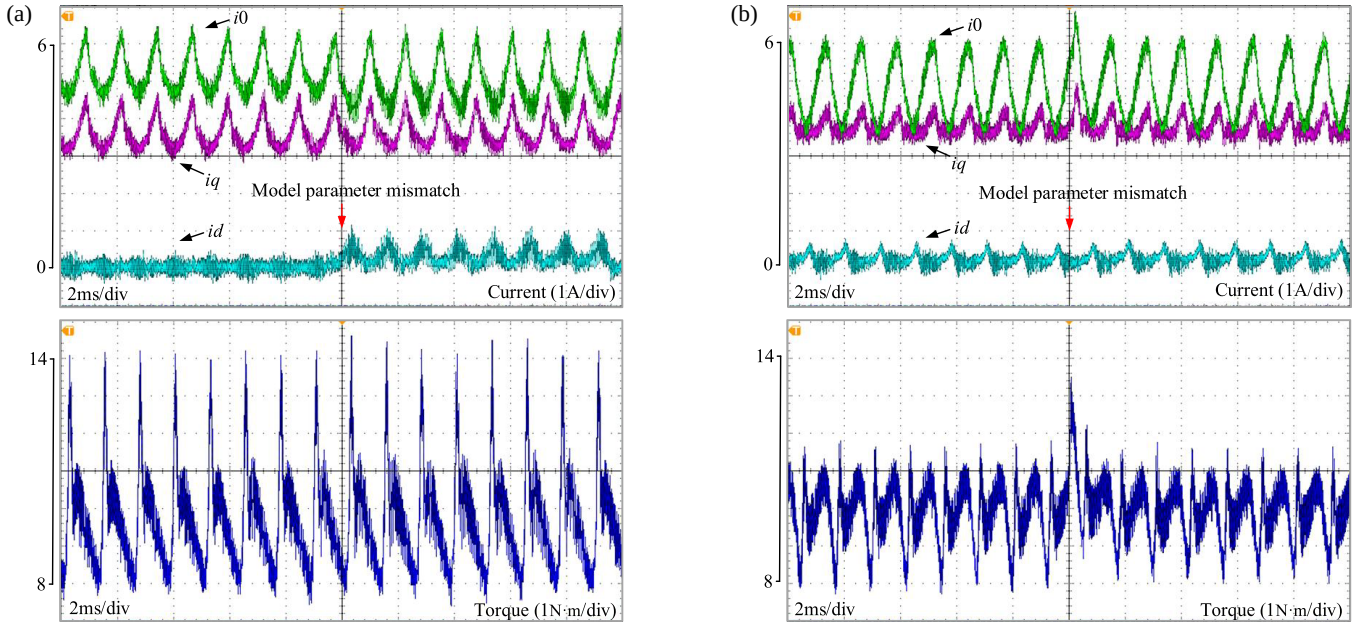

FIGURE 10. Comparison of experimental results at 1000 r/min with a 10 N·m load when model parameters are mismatched: (a) Traditional DPCC; (b) ASMC-DPCC.

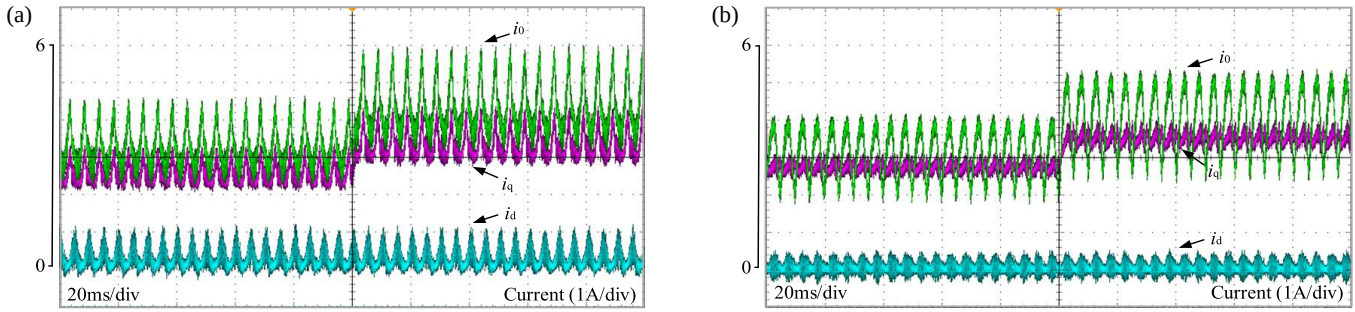

FIGURE 11. Comparison of experimental results of load torque step change at 5000 r/min: (a) Traditional DPCC; (b) ASMC-DPCC.

Overall, the presence of inductive mismatch leads to dramatic oscillations in the actual current of the conventional DPCC. The i_d current ripple increases from 0.83 A to 1.26 A, representing a surge of 51.8%. Similarly, the i_0 current ripple increases from 2.19 A to 2.68 A with an increase of 22.4%. However, under the control of the proposed ASMC-DPCC method, the *dq*0-axis currents show excellent mismatch resistance, and their current ripple increases are effectively suppressed to a low level of 1.9%, 2.4%, and 2.9%, respectively.

It is worth noting that model parameter mismatch also causes torque regulation problems in the deadbeat controller. The torque ripple of the conventional DPCC further deteriorates from 60.5% to 65.6% under the model parameter mismatch condition. In contrast, the proposed DPCC method with an anti-disturbance sliding mode controller is able to compensate the unknown disturbance components of the system in real time. As a result, the current ripple caused by model parameter mismatch is eliminated, and the deterioration of torque ripple is further effectively suppressed.

Finally, under conditions of model parameter mismatch, experimental comparisons are conducted between the two control methods for load torque step changes. Fig. 11 shows the dynamic response characteristics of the *dq*0-axis current to load torque step changes when the given speed is 500 r/min.

As can be seen from the results in Fig. 11, during the sudden change in load torque from 5 N·m to 8 N·m, the dynamic response times of the two methods are similar, and both exhibit good dynamic performance. It is worth noting that even under conditions of model parameter mismatch, the proposed ASMC-DPCC still maintains robust stability.

6. CONCLUSION

In this article, a sliding mode-based deadbeat predictive current control is proposed to realize the current and torque control of SRM drive system under model parameter mismatch. The method realizes high-precision control through dual inner-loop cooperative control. The first loop integrates the sliding mode torque-to-current converter into a standard DPCC sys-

tem, which provides a reference current for the deadbeat controller through the torque-to-current inverse mapping to realize torque control. The second loop designs the sliding mode deadbeat controller to suppress the current tracking error by dynamically compensating the voltage deviation to improve the robustness of the current control. The two controllers are designed with a unified sliding mode convergence law to ensure the dynamic steady-state response synergy. Simulation results show that ASMC-DPCC method exhibits lower torque ripple than the conventional DPCC scheme under medium and high-speed operating conditions, regardless of model parameter matching. In addition, ASMC-DPCC method not only significantly improves the current tracking performance and reduces current ripple, but also further optimizes the torque control performance under parameter mismatch conditions.

REFERENCES

[1] Cheng, H., S. Liao, and W. Yan, "Development and performance analysis of segmented-double-stator switched reluctance machine," *IEEE Transactions on Industrial Electronics*, Vol. 69, No. 2, 1298–1309, 2022.

[2] Fang, G., F. P. Scalcon, D. Xiao, R. P. Vieira, H. A. Gründling, and A. Emadi, "Advanced control of switched reluctance motors (SRMs): A review on current regulation, torque control and vibration suppression," *IEEE Open Journal of The Industrial Electronics Society*, Vol. 2, 280–301, 2021.

[3] Wang, S.-C. and Y.-H. Liu, "A modified PI-like fuzzy logic controller for switched reluctance motor drives," *IEEE Transactions on Industrial Electronics*, Vol. 58, No. 5, 1812–1825, 2011.

[4] Song, S., J. Liu, Y. Zhao, L. Ge, R. Ma, and W. Liu, "High-dynamic four-quadrant speed adjustment of switched reluctance machine with torque predictive control," *IEEE Transactions on Industrial Electronics*, Vol. 69, No. 8, 7733–7743, 2022.

[5] Ye, J., P. Malysz, and A. Emadi, "A fixed-switching-frequency integral sliding mode current controller for switched reluctance motor drives," *IEEE Journal of Emerging and Selected Topics in Power Electronics*, Vol. 3, No. 2, 381–394, 2015.

[6] Zhang, X., Q. Yang, M. Ma, Z. Lin, and S. Yang, "A switched reluctance motor torque ripple reduction strategy with deadbeat current control and active thermal management," *IEEE Transactions on Vehicular Technology*, Vol. 69, No. 1, 317–327, 2020.

[7] Ahmad, S. S., M. Thirumalasetty, and G. Narayanan, "Predictive current control of switched reluctance machine for accurate current tracking to enhance torque performance," *IEEE Transactions on Industry Applications*, Vol. 60, No. 1, 1837–1848, 2024.

[8] Valencia, D. F., R. Tarvirdilu-Asl, C. Garcia, J. Rodriguez, and A. Emadi, "A review of predictive control techniques for switched reluctance machine drives. Part I: Fundamentals and current control," *IEEE Transactions on Energy Conversion*, Vol. 36, No. 2, 1313–1322, 2021.

[9] Ge, L., Z. Fan, N. Du, J. Huang, D. Xiao, and S. Song, "Model predictive torque and force control for switched reluctance machines based on online optimal sharing function," *IEEE Transactions on Power Electronics*, Vol. 38, No. 10, 12 359–12 364, 2023.

[10] Sahoo, S. K., S. K. Panda, and J. X. Xu, "Iterative learning-based high-performance current controller for switched reluctance motors," *IEEE Transactions on Energy Conversion*, Vol. 19, No. 3, 491–498, 2004.

[11] Xia, Z., B. Bilgin, S. Nalakath, and A. Emadi, "A new torque sharing function method for switched reluctance machines with lower current tracking error," *IEEE Transactions on Industrial Electronics*, Vol. 68, No. 11, 10 612–10 622, 2021.

[12] Alharkan, H., S. Saadatmand, M. Ferdowsi, and P. Shamsi, "Optimal tracking current control of switched reluctance motor drives using reinforcement Q-learning scheduling," *IEEE Access*, Vol. 9, 9926–9936, 2021.

[13] Xia, Z., G. Fang, D. Xiao, A. Emadi, and B. Bilgin, "An online torque sharing function method involving current dynamics for switched reluctance motor drives," *IEEE Transactions on Transportation Electrification*, Vol. 9, No. 1, 534–548, 2023.

[14] Peng, F., J. Ye, and A. Emadi, "A digital PWM current controller for switched reluctance motor drives," *IEEE Transactions on Power Electronics*, Vol. 31, No. 10, 7087–7098, 2016.

[15] Liu, D., Y. Fan, J. Liu, G. Wang, and D. Sun, "Deadbeat indirect torque control of switched reluctance motors with current vector decomposition," *Journal of Electrical Engineering & Technology*, Vol. 19, No. 8, 4953–4968, 2024.

[16] Liu, D., Y. Fan, J. Liu, G. Wang, and L. Sheng, "Robust deadbeat predictive current control for unipolar sinusoidal excited SRM with multi-parameter mismatch compensation," *Scientific Reports*, Vol. 14, No. 1, 23746, 2024.

[17] Liu, J., G. Wang, D. Liu, and Y. Fan, "An improved deadbeat control scheme for unipolar sinusoidal current excited switched reluctance motor drives," *IEEE Journal of Emerging and Selected Topics in Power Electronics*, Vol. 11, No. 2, 1589–1603, 2023.

[18] Jiang, Y., W. Xu, C. Mu, and Y. Liu, "Improved deadbeat predictive current control combined sliding mode strategy for PMSM drive system," *IEEE Transactions on Vehicular Technology*, Vol. 67, No. 1, 251–263, 2018.

[19] Nakao, N. and K. Akatsu, "Vector control specialized for switched reluctance motor drives," in *2014 International Conference on Electrical Machines (ICEM)*, 943–949, Berlin, Germany, 2014.

[20] Ding, W., J. Li, and J. Yuan, "An improved model predictive torque control for switched reluctance motors with candidate voltage vectors optimization," *IEEE Transactions on Industrial Electronics*, Vol. 70, No. 5, 4595–4607, 2023.